Temperature Dependence of the Low-Field Galvanomagnetic Coefficients of Bismuth

ROBERT HARTMAN*
Research Division, IBM Watson Laboratory, Columbia University, New York, New York 10025
(Received 30 September 1968)

The linear Hall and quadratic magnetoresistance coefficients of bismuth have been measured as functions of temperature in the range 4–16°K. The sensitivity ($\sim 10^{-12}$ V) and accuracy (1 part in 10^4) necessary for the experiment required the construction of an automatically balancing superconducting-chopper picovolt potentiometer, together with a cryogenic system which was stable to 1 part in 10^6 at any value of temperature in the range 4–16°K. The zero-field resistivities ρ_{11}^0 and ρ_{33}^0, normal and parallel to the trigonal direction, respectively, have been measured to 26°K. Both ρ_{33}^0 and ρ_{11}^0 are closely proportional to T^2 between 8 and 20°K. All eight magnetoresistance coefficients have an approximate T^{-2} dependence, while the large Hall term $\rho_{23,1}$ decreases approximately 7% as the temperature increases from 6 to 16°K. A least-squares fit of the data to a model based on the accepted band structure of bismuth was made at each temperature. From these, experimental values for the carrier density and the components of the mobility tensors for electrons and holes were obtained as a function of temperature. The carrier density, constant with temperature, is 2.7×10^{17} electrons per cm^3, and an equal hole density. All the mobility components varied as T^{-2} in the temperature range 8–16°K. At 4.2 the electron mobilities are (in 10^7 cm^2/V sec) $\mu_1=11$, $\mu_2=0.3$, $\mu_3=6.7$, $\mu_4=-0.71$, $\nu_1=2.2$, and $\nu_3=0.35$. The mobility tilt angle is a constant, $\theta_\mu=6.2°$, in the temperature range 4.2–16°K. The components of the conductivity relaxation-time tensor were calculated for the electrons and holes at each temperature. At 4.2°K the maximum anisotropy of the electron relaxation-time tensor was found to be 5:1, decreasing rapidly as the temperature increased, while the anisotropy of the hole tensor was 2:1 over the entire temperature range. At 4.2°K the diagonal components of the electron and hole relaxation-time tensors are (in units of 10^{-10} sec): $\tau_{1e}=4.4$, $\tau_{2e}=22$, $\tau_{3e}=4.4$, $\tau_{1h}=8.5$, and $\tau_{3h}=15$. Because the conductivity varies as T^{-2}, we argue that the dominant scattering is not deformation-potential scattering, but rather is between carriers in separate valleys. The carriers in different valleys interact via the Coulomb interaction, each remaining in its respective valley, conserving energy and momentum in the center-of-mass system, though not individually. For carriers of differing charge or of sufficient anisotropy, this mechanism contributes to the resistivity. In support of this mechanism, the electron and hole mobilities at 4.2°K were estimated, from the known ionized-impurity scattering, to be $\mu_e=9\times 10^7$ cm^2/V sec and $\mu_h=0.6\times 10^7$ cm^2/V sec, in very good agreement with the measured mobilities.

I. INTRODUCTION

NUMEROUS studies[1] have been made of the electronic properties of bismuth, a Group-V semimetal. It is known[2] that at low temperatures there are 2.9×10^{17} electrons/cm^3 distributed among geometrically equivalent conduction-band minima located at the L points[3] in the reduced Brillouin zone (Bz) (see Fig. 1) and an equal number of holes (within $\pm 5\%$) [2] at the T points. The electron Fermi surface[2] is well approximated by a set of three highly prolate ellipsoids, centered at the L points, occupying $\sim 10^{-5}$ of the volume of the reduced zone, so that a typical linear dimension of the Fermi surface is $\sim 1\%$ of the Bz dimension. One axis of each ellipsoid is parallel to a crystal axis of twofold rotational symmetry (a binary axis), the other two principal axes of each ellipsoid lie in mirror planes and are tilted[4] from the axis of threefold rotational symmetry (the trigonal axis) by $\sim +6°$. The electron-energy dispersion relation is nonparabolic below the Fermi energy of 25 meV. There is a direct energy gap of 15 meV to a lower filled band at the L points. The hole Fermi surface[2] is known to be an ellipsoid of revolution about the trigonal axis. The hole-energy dispersion relation is parabolic below the Fermi energy of 11 meV.

Measurements of the electrical conductivity at low temperatures by Friedman,[5] which are in agreement with a summary of data compiled by Zitter[6] (and a conjecture by White and Woods[7]) clearly show that at low temperatures the bulk conductivity of the pure material is closely proportional to T^{-2}. Since the typical wavelength of an electron or hole is comparable to or larger than the lattice spacing, the main criteria for the applicability of the deformation potential treatment of electron-lattice scattering is satisfied. Such an analysis has been used by Mase *et al.*[8] to fit extensive high-field galvanomagnetic data at 20.4°K. At low temperatures the deformation potential approach predicts a mobility proportional to T^{-1}, similar to the prediction of the Bloch-Gruneisen formula for simple metals, but contrary to the observed T^{-2} behavior of the conductivity. Since the bismuth Fermi surface is highly anisotropic,

* Present address: Bell Telephone Laboratories, Murray Hill, N. J.

[1] An extensive bibliography of the older references can be found in A. L. Jain and S. H. Koenig, Phys. Rev. **127**, 442 (1962). More recent references are in R. N. Bhargava, Phys. Rev. **156**, 785 (1967).

[2] R. N. Bhargava, Ref. 1.

[3] S. H. Koenig, A. A. Lopez, D. B. Smith, and J. L. Yarnell, Phys. Rev. Letters **20**, 48 (1968).

[4] R. D. Brown, III, R. L. Hartman, and S. H. Koenig, Phys. Rev. **172**, 598 (1968).

[5] A. N. Friedman, Phys. Rev. **159**, 553 (1967).

[6] R. N. Zitter, Phys. Rev. **127**, 1471 (1962).

[7] G. K. White and S. B. Woods, Phil. Mag. **3**, 341 (1958).

[8] S. Mase, S. Van Molnar, and A. W. Lawson, Phys. Rev. **127**, 1030 (1962).

it is conceivable that the temperature dependence of the various components of the mobility tensor are different. The conductivity, which is a linear combination of the components of the mobility tensor, might then have a resultant T^{-2} behavior.

Thus, a knowledge of the temperature dependence of each of the components of the mobility tensors is necessary to clarify the problem. Such information can be obtained most directly by a complete set of galvanomagnetic measurements in the low-temperature range. A set of these measurements, from which the carrier mobilities and information about the carrier concentrations can be directly calculated, was performed at temperatures between 4.2 and 16°K. Zitter[6] has enumerated some of the experimental difficulties. Briefly, the low magnetic field condition (see Sec. II) which restricts the applied magnetic fields and the sample current (because of the self-magnetic field) limits the magnitude of the available signals. The detection of these small signals requires a voltmeter which is sensitive to $\sim 10^{-12}$ V dc and accurate to 1 part in 10^4. An automatic-balancing superconducting-chopper potentiometer, which achieved this sensitivity and accuracy, was designed and built, making it possible to determine the temperature dependence of the mobilities and carrier concentrations. Additional difficulties were caused by the large distance required between the chopper and the sample (so that the superconducting elements would not distort the field at the sample), and by the large thermoelectric power ($\sim 10^{-5}$ V/°K) of bismuth which required a temperature stability in the sample chamber of 1 part in 10^6. This stability was achieved with a feedback temperature controller and a special isothermal chamber.

Section III is a brief description of the experimental apparatus. A more complete description has been described elsewhere.[9] The measurement procedures are described in Sec. IV. The results of the measurements (see Sec. V) are then used to calculate the mobilities and to deduce the relaxation time tensor. Finally, conclusions are drawn (Sec. VI) about the dominant scattering mechanism, which is peculiar to bismuth.

II. THEORY

The phenomenological theory of low-field galvanomagnetic effects in bismuth has already been described.[6,10–12] It is summarized here (with the errors in the literature corrected) in the notation used by Brown *et al.*[4] The theory assumes Ohm's law to hold for the conductivity tensor $\boldsymbol{\sigma}(\mathbf{B})$ or its reciprocal, the resistivity tensor $\boldsymbol{\rho}(\mathbf{B})$, in the presence of a magnetic induction field $\mathbf{B}$. In an anisotropic media these relations can be written

$$J_j=\sum_i \sigma_{ji}(\mathbf{B})\mathcal{E}_i,$$

$$\mathcal{E}_j=\sum_i \rho_{ji}(\mathbf{B})J_i,$$

where $\boldsymbol{\mathcal{E}}$ is the electric field and $\mathbf{J}$ the current density. $\boldsymbol{\sigma}(\mathbf{B})$ and $\boldsymbol{\rho}(\mathbf{B})$ are then expanded in powers of $\mathbf{B}$, assuming the expansions will converge if $\mathbf{B}$ is small enough. The tensors $\boldsymbol{\sigma}(\mathbf{B})$ and $\boldsymbol{\rho}(\mathbf{B})$ must be invariant under the point group symmetry operations of the crystal and must satisfy the Onsager reciprocal relations. These two conditions restrict the number of nonzero elements in the tensor coefficients of the expansions. The group-theoretical analysis has been given by Juretschke[13] and Okada.[12] For clarity, the nonzero elements of the matrices are explicitly written out in Eqs. (A1) and (A2) of Appendix A. Apart from sign, all our nonzero tensor components are equal in magnitude to the subscripted letters which are used as their counterparts in the papers of Juretschke, Okada, or Zitter.[14] There are a total of 12 independent tensor components in Eqs. (A1) and (A2).

Abeles and Meiboom[11] have calculated the 12 conductivity tensor components for bismuth for an ellipsoidal model of the Fermi surface which assumes that intravalley processes dominate the scattering, that the collision integrals can be approximated by a relaxation time,[15] and that the tilt is zero. They obtained the vector current density contribution of each constant energy ellipsoid and then summed these vectors in the frame of the crystal axes. Assuming an isotropic relaxation time τ, they obtained

$$\mathbf{J}=\boldsymbol{\sigma}^0\cdot[\boldsymbol{\mathcal{E}}+(nec)^{-1}\mathbf{J}\times\mathbf{B}] \tag{1}$$

from the Boltzmann equation. Here n is the carrier concentration per ellipsoid and the conductivity tensor $\boldsymbol{\sigma}^0=ne\boldsymbol{\mu}=ne^2\tau\boldsymbol{\alpha}$, where $\boldsymbol{\mu}$ is the mobility tensor and $\boldsymbol{\alpha}$ the reciprocal-effective-mass tensor. This equation can be solved for $\mathbf{J}$:

$$\mathbf{J}=ne[\boldsymbol{\delta}\mp(\boldsymbol{\mu}\cdot\mathbf{B})/c]^{-1}\cdot\boldsymbol{\mu}\cdot\boldsymbol{\mathcal{E}},$$

where $e=|e|$, the upper sign is for electrons, and the lower sign for holes. $\boldsymbol{\delta}$ is the unit tensor and $\mathbf{B}$ the skew-symmetric matrix form of the vector $\mathbf{B}$. In this form, the equation shows that we can perform the required expansion of $[\boldsymbol{\delta}\mp(\boldsymbol{\mu}\cdot\mathbf{B})/c]^{-1}$ for the conductivity tensor if the magnitude of each term of $(\boldsymbol{\mu}\cdot\mathbf{B})/c<1$. (This can be proven by solving iteratively for each component of the current using $\mathbf{J}\cdot[\boldsymbol{\delta}\mp(\boldsymbol{\mu}\cdot\mathbf{B})/c]=ne\boldsymbol{\mu}\cdot\boldsymbol{\mathcal{E}}$.) This is also

[9] R. L. Hartman, IBM Research Report No. RW105 (unpublished), available from the author.
[10] J. Okada, J. Phys. Soc. Japan **12**, 1327 (1967).
[11] B. Abeles and S. Meiboom, Phys. Rev. **101**, 544 (1956).
[12] J. Okada, Mem. Fac. Sci., Kyushu Univ. **B1**, 168 (1955).
[13] H. J. Juretschke, Acta. Cryst. **8**, 716 (1955).
[14] The nonzero tensor components agree in sign with Okada's terms; the signs of Juretschke's A_{24} and A_{42} are opposite to our corresponding terms A_{14} and A_{41}; Zitter appears to have changed from Okada's sign for his formulas (12)–(17) to Juretschke's signs in the theory, causing the error in the signs of his terms $\rho_{11,23}$ and $\rho_{23,11}$ listed in the Appendix to his paper.
[15] C. Herring and E. Vogt, Phys. Rev. **101**, 944 (1956).

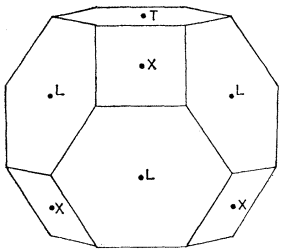

FIG. 1. Reduced Brillouin zone for bismuth.

the condition that $\omega\tau<1$, where ω is the cyclotron frequency. Zitter,[6] using the results of Herring and Vogt,[15] extended the analysis to a nonisotropic relaxation-time tensor $\boldsymbol{\tau}(E)$ and allowed for a tilt of the ellipsoidal Fermi energy surfaces.

For the model of bismuth presented in Sec. I, the mobility tensor for each electron ellipsoid may be written

$$\mathbf{\mu}=\begin{pmatrix}\mu_1 & 0 & 0\\ 0 & \mu_2 & \mu_4\\ 0 & \mu_4 & \mu_3\end{pmatrix}, \tag{2}$$

and a mobility tensor for the hole ellipsoid

$$\boldsymbol{\nu}=\begin{pmatrix}\nu_1 & 0 & 0\\ 0 & \nu_1 & 0\\ 0 & 0 & \nu_3\end{pmatrix}. \tag{3}$$

This representation of $\mathbf{\mu}$ and $\boldsymbol{\nu}$ uses as a basis a binary, bisectrix, and trigonal triad as the x, y, and z directions, respectively, centered at L (Fig. 1) for each ellipsoid. (The bisectrix is defined as the third direction necessary to complete a right-handed triad.) One major axis of the ellipsoid associated with $\mathbf{\mu}$ is along the x direction. The other two major axes are tilted (i.e., rotated about the x axis in the sense **2×3**) by an angle θ_μ given by[16]

$$\tan 2\theta_\mu=2\mu_4/(\mu_2-\mu_3). \tag{4}$$

The z axis of the hole mobility ellipsoid is coincident with the trigonal direction, which is an axis of revolution for this ellipsoid. All the mobility components are intrinsically positive except μ_4; its sign depends upon the sign of $2\theta_\mu$ and is obtained from the measurements of A_{14} and A_{41}. There are no *a priori* reasons for the principal axes of $\boldsymbol{\tau}$ to be coincident with those of $\boldsymbol{\alpha}$, though Herring and Vogt[15] assume this condition in their theory of anisotropic scattering. As Zitter[6] has pointed out, since the Herring and Vogt work only involves the product $\boldsymbol{\tau}\cdot\boldsymbol{\alpha}$, their theory can be trivially extended to the case where $\boldsymbol{\tau}$ and $\boldsymbol{\alpha}$ have noncoincident principal axes.

The total conductivity is obtained in the present representation by adding the currents from: (1) the hole ellipsoid, (2) one of the electron ellipsoids where $\mathbf{\mu}$ is given by Eqs. (2), and (3) the other two electron ellipsoids rotated into this frame by a $\pm 120°$ rotation about the trigonal axis. The form of this last contribution becomes

$$ne\mathbf{R}\cdot\{[\boldsymbol{\delta}-\mathbf{\mu}\cdot\mathbf{R}^{-1}\cdot\mathbf{B}/c]^{-1}\cdot\mathbf{\mu}\}\cdot\mathbf{R}^{-1}, \tag{5}$$

where $\mathbf{R}$ is the rotation matrix given by Abeles and Meiboom[11] and $e=|e|$. The results for the total conductivity tensor are given in Appendix B, in mks units. They are the same as Zitter's[6] results except for the changes required by notational differences. For the model used here, the total electron density N should equal the hole density P. However, in Appendix B their ratio $c=P/N$ is not assumed equal to unity, *a priori*.

Experimentally, the current density is the independent variable, since its direction is determined by the geometry of the sample. It is more convenient, therefore, to measure the resistivity tensor components, and to have them expressed in terms of the mobility. The appropriate equations are also in Appendix B. They differ from Zitter's expressions (which we believe contain algebraic errors), particularly with regard to the signs of some of the terms.

There are eight independent variables in the model (μ_1, μ_2, μ_3, μ_4, ν_1, ν_3, P, and N) and 12 nonzero tensor components of either $\boldsymbol{\sigma}$ or $\boldsymbol{\varrho}$ to order B^2. Therefore, there must be four identities among the tensor components as discussed by Zitter, who pointed out that two of these identities (equivalent in form to two used by Epstein and Juretschke[17]) are particularly simple and can be useful for checking the internal consistency of the experimental data. They are

$$S_{12}+2S_{33}=3S_{11}-2S_{44}, \tag{6}$$

$$S_{11}+4[(\sigma_{23,1}S_{13}/\sigma_{12,3})+(\sigma_{11}{}^0S_{31}/\sigma_{33}{}^0)]$$
$$=3S_{12}-S_{44}[2+(8\sigma_{11}{}^0\sigma_{23,1}/\sigma_{12,3}\sigma_{33}{}^0)]. \tag{7}$$

Another test of the data[6] is the sign computed for S_{44} (cf. Appendix B), which for the model used must be negative. However, in terms of measured quantities (cf. Appendix C),

$$(1/\rho_{11}{}^0\rho_{33}{}^0)[A_{44}-(\rho_{12,3}\rho_{23,1}/2\rho_{11}{}^0)]=S_{44}<0, \tag{8}$$

which imposes another consistency restriction on the data.

To obtain the parameters of the model from the measured resistivity tensor components is a difficult task, as noted by previous authors.[6,18] Two procedures may in principle be used: One could solve Eqs. (B2) for the parameters of the model and then substitute the measured quantities into the resulting complicated algebraic expressions, or one could take various trial values of the model parameters and using Eqs. (B2), compute the expected values of the parameters that were measured, and compare these with the measurements. We have taken the latter approach and used a

[16] Cf. Ref. 4.

[17] S. Epstein and H. J. Juretschke, Phys. Rev. **129**, 1148 (1963).

[18] S. J. Freedman and H. J. Juretschke, Phys. Rev. **124**, 1379 (1961).

generalized least-squares fit of the measurements to the prediction of Eqs. (B2). While the larger terms of the measured ρ were the most precisely determined, their magnitude would have masked the contribution of the smaller terms if a simple minimization of the sum of the squared residuals were used. To obviate this difficulty, a program was written to minimize a weighted least-squares percentage residual function using the variable metric method by Davidon.[19] The function minimized was

$$f(x_i)=\sum_{j=1}^{12}[\omega_j R_j(1-C_j/R_j)]^2, \qquad (9)$$

$i=1, \cdots, 8$; R_j is the measured value of the jth term, ω_j the jth weight factor, C_j the calculated value of the jth term using Eqs. (B2), and x_i, $i=1, \cdots, 8$, the eight variables, i.e., parameters of the model. The weighting factors for this function are related in a simple way to the percentage uncertainties of the different measurements. Using a base of 100 and an estimated percentage error in the ith term, P_i, $\omega_i=100/P_i$.

Included in the program was the facility to constrain any of the variables, a feature that was used in a way which will be discussed later. The program was run on IBM 7094 and 360-50 computers; a typical minimization required a few minutes of computation time.

III. EXPERIMENTAL DETAILS

Figure 2 is a block diagram of the electronics. The system can be regarded as a high-gain amplifier (open loop gain $A\simeq 10^{19}$) stabilized by feeding back a sizable fraction $(1-\beta)$ of the output, where $\beta=R_H/(R_R+R_H)\simeq 10^{-9}$. Then the ratio of output to input voltage $e_0/e_i\simeq(1-1/A\beta)\beta^{-1}$. Input signals of the form $e_i=e_i^0+e_{i1}(\mu B)+e_{i2}(\mu B)^2+\cdots$, where $\mu B<1$, have to be measured to 1% in the squared term, corresponding to 1 part in 10^4 in $e_i\simeq 10^{-8}$ V dc. The over-all requirement is that the apparatus sense $\sim 10^{-12}$ V dc, and have a closed-loop gain stable to at least 1 part in 10^4, i.e., $A\beta>10^4$.

The input circuitry utilized a superconducting chopper, a cryotron,[20] to detect the small galvanomagnetic voltages generated across a bismuth sample. This was an extension of earlier work of Templeton,[21] later improved by Vroomen and van Baarle,[22] Zitter,[6] and Kachinskii.[23] The cryotron has the advantage of a low noise level [$<10^{-11}$V/Hz$^{1/2}$], and the ability to interrupt a dc signal in any circuit with internal impedance much lower than the cryotron gate resistance in its normal state ($\sim$0.1 Ω). In our case, the resistance

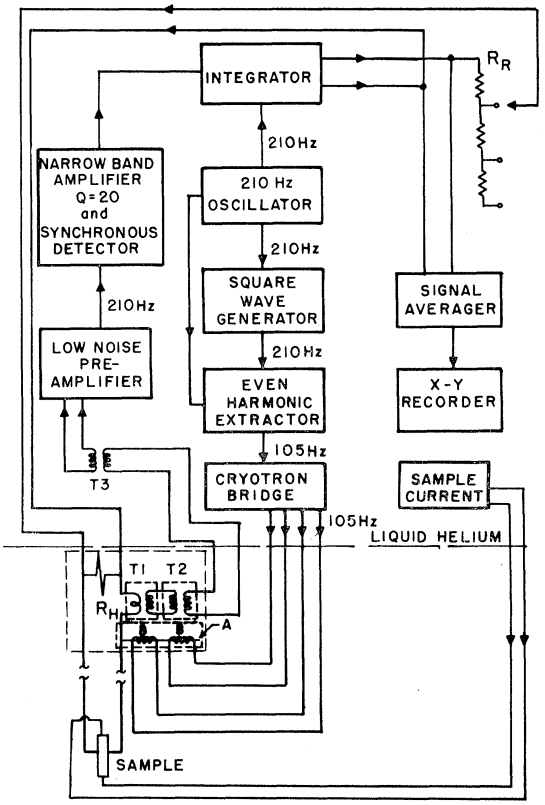

FIG. 2. Block diagram of the picovolt potentiometer. A is the gate and B the control coils of the cryotron. R_H is the calibrated resistor in liquid helium and R_R the feedback or mode control resistor. $T1$, $T2$, and $T3$ are primary transformers. The dashed lines are superconducting shields.

of the samples varied between 10^{-7} and 10^{-4} Ω. (The device recently described[24] based on the Josephson effect does not have the required voltage sensitivity at these high impedance levels.) The bucking resistor $R_H\sim 10^{-5}$ Ω was calibrated in liquid helium with special care taken to keep the calibrating current sufficiently low to prevent heating of R_H.

The major improvement in the present work was achieved by modifying the cryotron so that the control current flowed through two adjacent identical solenoids wound in series opposition, and by using a carefully shaped cryotron control current free of second harmonics to 1 part in 10^6.

The requirement that $A\beta\geq 10^4$ is equivalent, for a simple feedback circuit, to setting the ratio of the first two time-ordered time constants, $\tau_1/\tau_2\simeq 10^4$. The τ_1 and τ_2 for the system (Fig. 2) are determined by the integrator and narrow band amplifier, respectively, provided the transformers $T1$, $T2$, and $T3$ are sufficiently wide band. The bandwidth of the transformer network is limited by the leakage inductance of $T1$, which was increased 300% through the use of a close-

[19] W. C. Davidon, Argonne National Laboratory Report No. ANL-5990 Rev. Phys. and Math. TID-4500, 14th ed., 1959 (unpublished).
[20] D. A. Buck, Proc. IRE 44, 482 (1956).
[21] I. M. Templeton, J. Sci. Instr. 32, 314 (1955).
[22] A. R. de Vroomen and C. van Baarle, Physica 23, 705 (1957).
[23] V. N. Kachinskii, Pribory i Tekhn. Eksperim. 5, 207 (1963).
[24] J. Clark, Phil. Mag. 13, 115 (1960).

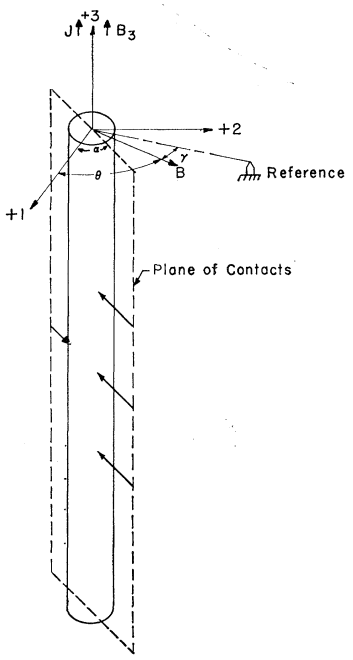

FIG. 3. The trigonal crystal and its relation to **B** and the angles θ, α, and γ.

fitting superconducting shield which forced the flux lines back into the core of $T1$.

The perturbation of the uniform magnetic field applied to the sample (due to the Meissner effect of the superconducting shields placed about the input circuitry) was kept below $\sim 0.1\%$ by displacing the input circuitry ~ 30 cm from the sample. Superconducting ribbon with 10^{-11} H/cm inductance were used to connect the sample to the input circuit.

There is an isothermal sample chamber, thermally isolated from, but contained within, a low thermal conductivity vacuum tight chamber in contact with the helium bath. The isothermal chamber was designed to minimize the effects of the large thermoelectric power of bismuth. Fluctuations of 1 part in 10^6 in any temperature gradients along the sample would be detectable as electrical signals, and larger fluctuations would obscure the desired signal. These fluctuations were minimized by minimizing the thermal contact of the sample chamber (e.g., leads, supports) with its external environment and by stabilizing the temperature of the chamber. The temperature was controlled by a servo system using a heater and a resistance thermometer. By careful attention to the thermal time constants and appropriate lead circuitry in the servo amplifier, it was possible to achieve a temperature stability of 1 part in 10^6. As a result of these numerous precautions, the voltage produced by the thermal gradient over the temperature range 4.2–16°K varied from negligible to 8% of the voltage generated by the sample in zero field.

The sensing resistor was calibrated against another resistor[25] in turn calibrated in the range 4–20°K against a constant-volume helium-gas thermometer; the resultant temperature uncertainty is $\pm 0.25\%$.

The condition $\mu B/c \leq 1$, discussed previously, limited the magnetic field strength to a maximum of 2 G. The magnetic field of the earth and other stray magnetic fields had to be reduced to $\sim 1\%$ of the smallest fields used. For this purpose, three mutually perpendicular pairs of square coils, 2 ft on a side and 1 ft apart, were constructed. The measured stray magnetic field was ~ 0.4 G and fluctuated ~ 4 mG during the day and somewhat less at night. The coils were set to buck out the average field with no attempt to eliminate these fluctuations. A rotatable Helmholtz coil was used to produce a known horizontal magnetic field component and an end compensated solenoid was used to generate a vertical magnetic field component in this otherwise field-free region. The rotation axis of the Helmholtz coils was made to coincide with the axis of the solenoid within $\pm 0.1°$ and the longitudinal axis of the sample within $\pm 0.3°$.

A power supply which could be swept at a preselected constant rate was designed to provide the current for the solenoid and the Helmholtz coils. The maximum magnetic field sweep rate was limited by the time constant of the signal averager (Fig. 2).

The self-magnetic field caused by the sample current was never greater than 1% of the smallest applied magnetic fields.

A crystal was grown from 10 kg of 99.9999% bismuth (obtained from Cominco Products, Inc.) following the modified Bridgeman technique described by Brown.[26] Nine meltings and recrystallizations produced a boule which was composed almost entirely of one single crystal.

A trigonal plane was obtained for mounting by cleaving the crystal either under water or liquid nitrogen. A slight acid etch of this plane revealed sets of line at 60° to each other, corresponding to the binary directions.[4] Two cylindrical single-crystal samples approximately 7 cm long and 0.7 cm in diameter, one sample with the axis of the cylinder along the binary direction, the other along the trigonal direction, were spark-cut from the crystal. A copper block spark-cut concentric with the sample surface and colinear with the sample axis was used as a support so that the problem of crystal misalignment was minimized. The correct crystallographic orientation of the samples were determined by both Laue photographs and examination of the secondary cleavage planes, in the manner described in detail by Brown *et al.*[4]

Each sample was placed in a jig designed to position copper probe contacts on the sample in the usual four probe galvanomagnetic configuration; two longitudinal

[25] This calibrated resistor was kindly supplied by Dr. A. A. Lopez.

[26] R. D. Brown, III, IBM J. Res. Develop. **10**, 462 (1966).

contacts, separated by 2 cm, and two transverse contacts centered on the sample.

The ratio of room-temperature resistance to liquid-helium resistance was $R_{300}/R_{4.2}\simeq 460$ for the trigonal crystal, and $\simeq 360$ for the binary. These fairly high ratios, together with a measured ratio of 580 for a crystal grown from the same 99.9999% initial material but regrown 60 times, indicate that each regrowth yielded purer samples in a manner similar to zone refining.

The mounting and cutting procedures outlined above were designed to minimize any error in crystal alignment to the angular error between the cleaved trigonal plane and the true plane. Previous experiments by the author comparing a cleaved trigonal plane to the trigonal plane determined by x rays showed that any angular differences that occurred were less than 1°.

IV. MEASUREMENT PROCEDURES

Data were taken on two cylindrical crystals, one with the current along the trigonal (3) axis (trigonal sample) and one with current along the binary (1) axis (binary sample). Cylindrical samples had the advantage that the orientation of the bisectrix axis for each sample could be accurately determined from the galvanomagnetic data.

Equations (10)–(13) relate the galvanomagnetic tensor components to the transverse voltage V_T and the longitudinal voltage V_L. For the trigonal sample [cf. Eqs. (10) and (11) and Fig. 3], θ is the angle between a binary axis and the component of the magnetic field in the trigonal plane, α is the angle between the line connecting the transverse probes and this binary axis, J is the current density, g_L and g_T are geometric factors which depend on the placement of the longitudinal and transverse contacts, B and B_3 are the magnitudes of the magnetic induction fields perpendicular and parallel to the current direction, and

$$V_{T,\mathrm{Trig}}=[-\rho_{23,1}B\sin(\theta-\alpha)+2A_{44}BB_3\cos(\theta-\alpha)+A_{41}B^2\sin(2\theta+\alpha)]Jg_T, \quad (10)$$

$$V_{L,\mathrm{Trig}}=(\rho_{33}{}^0+A_{31}B^2+A_{33}B_3{}^2)Jg_L. \quad (11)$$

For the binary sample, B_1 is the magnitude of the magnetic field component along the binary direction, and θ and α are measured from a bisectrix axis.

$$V_{L,\mathrm{Binary}}=\{\rho_{11}{}^0+A_{11}B_1{}^2+B^2[\tfrac{1}{2}(A_{12}-A_{13})\cos 2\theta+\tfrac{1}{2}(A_{12}+A_{13})+A_{14}\sin 2\theta]\}Jg_L, \quad (12)$$

$$V_{T,\mathrm{Binary}}=\{-\rho_{12,3}B\cos\alpha\sin\theta+\rho_{23,1}B\sin\alpha\cos\theta+BB_1[(2A_{14}\cos\alpha+2A_{44}\sin\alpha)\sin\theta+([A_{11}-A_{12}]\cos\alpha+2A_{41}\sin\alpha)\cos\theta]\}Jg_T. \quad (13)$$

Measurements were made either by varying the magnetic field strength with the magnetic field direction held fixed, and recording the output voltage versus field strength on an x-y recorder, or by rotating a magnetic field of fixed magnitude in a plane perpendicular to the long axis of the sample and recording the signal versus angular position of the magnetic field. In both cases, the zero field contribution to V_L and V_T was bucked out, usually by an added highly stable voltage (derived from mercury cells) inserted in the feedback loop of the measuring apparatus. All measurements were made for both directions of J, and the data averaged.

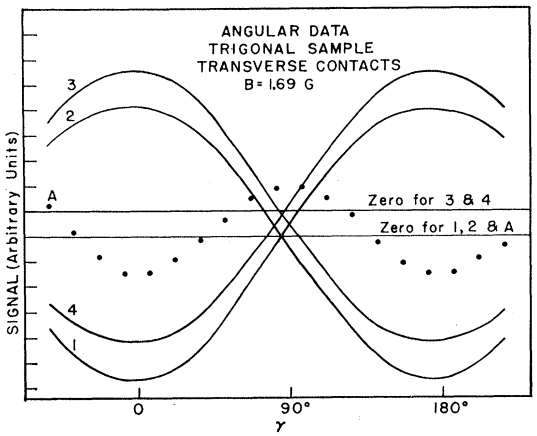

FIG. 4. Typical angular data for the transverse voltage. The solid smooth lines are the data as taken, the points (on a scale ten times larger) are the averages of the four curves, which are displaced for clarity.

We note for the trigonal sample, from Eq. (10), that if $B_3=0$, the dependence of $V_{T,\mathrm{Trig}}$ on θ has two terms, one linear in B with a period of 2π, the other quadratic in B with a period of π. These two terms can readily be separated from analysis of the angular dependence of V_T for fixed B. Once this is done, two directions of B (i.e., two values of γ, cf. Fig. 3) can be found, one such that $\sin(\theta-\alpha)=0$, the other such that $\sin(2\theta+\alpha)=0$.

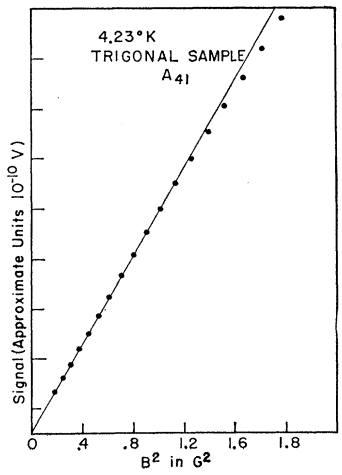

FIG. 5. Typical reduced magnetoresistance data for A_{41} with the four curves (not shown) of ± current and ± magnetic field already averaged.

TABLE I. The measured tensor components[a] and the components predicted by a two-carrier model with parameters obtained from a least-squares fit to the data.

Temperature (°K)	4.23	4.94	5.88	6.82	7.78	8.74	9.72	10.7	11.7	12.7	13.7	14.7	15.7
ρ_{11}^0													
Measured	2.91	3.36	4.44	5.79	8.07	10.3	13.0	15.9	19.1	22.5	26.2	30.0	34.0
Calculated	2.92	3.36	4.44	5.84	8.25	10.4	13.1	15.9	19.1	22.7	26.0	30.4	34.4
ρ_{33}^0													
Measured	3.21	3.86	4.83	6.27	8.45	10.7	13.4	16.5	20.4	24.2	28.5	32.9	37.5
Calculated	3.26	3.89	4.87	6.30	8.39	10.7	13.7	16.9	20.5	24.4	28.2	33.2	37.7
$\rho_{23,1}$													
Measured	1.54	1.56	1.58	1.59	1.57	1.57	1.55	1.54	1.53	1.52	1.50	1.47	1.44
Calculated	1.53	1.55	1.62	1.62	1.56	1.57	1.55	1.52	1.53	1.53	1.51	1.50	1.49
$\rho_{12,3}$													
Measured	−0.07	−0.06	−0.05	−0.05	−0.05	−0.04	−0.03	−0.02	−0.01	−0.01	+0.00	+0.00	+0.01
Calculated	−0.06	−0.03	−0.02	−0.02	−0.12	−0.12	−0.13	−0.14	−0.15	−0.15	−0.15	−0.16	−0.16
A_{11}													
Measured	35	32	27	21	16	13	9.6	7.5	6.2	5.1	4.4	3.7	3.1
Calculated	37	32	28	22	16	13	9.6	7.6	6.4	5.4	4.6	3.8	3.3
A_{12}													
Measured	48	43	33	25	18	14	11	9.0	7.4	6.1	5.1	4.4	3.8
Calculated	44	39	34	25	19	15	12	9.1	7.7	6.5	5.5	4.6	4.0
A_{13}													
Measured	12	9.6	7.3	5.0	3.1	2.4	1.8	1.4	1.1	0.97	0.82	0.72	0.61
Calculated	11	9.4	7.2	5.0	2.8	2.1	1.7	1.3	1.1	0.87	0.73	0.63	0.54
A_{31}													
Measured	38	32	26	19	15	12	9.7	8.0	6.8	5.9	5.0	4.3	3.8
Calculated	37	30	24	17	14	11	8.7	7.0	6.0	5.0	4.3	3.7	3.3
A_{33}													
Measured	3.3	2.5	2.0	1.6	1.2	1.0	0.73	0.56	0.48	0.41	0.34	0.30	0.26
Calculated	2.6	2.2	1.8	1.3	1.0	0.80	0.62	0.51	0.42	0.36	0.30	0.26	0.23
A_{14}													
Measured	9.3	6.2	4.0	2.6	1.8	1.5	1.2	1.0	0.8	0.7	0.57	0.47	0.40
Calculated	7.8	6.7	5.8	4.4	3.4	2.6	2.0	1.6	1.3	1.1	0.95	0.79	0.70
A_{41}													
Measured	4.5	3.8	3.6	2.6	2.1	1.5	1.2	0.95	0.80	0.67	0.57	0.49	0.43
Calculated	5.3	4.4	3.8	2.9	2.3	1.8	1.4	1.1	0.90	0.76	0.65	0.54	0.48
$-A_{44}$													
Measured	5.8	4.6	3.3	2.3	1.7	1.3	1.1	0.9	0.75	0.63	0.54	0.49	0.44
Calculated	6.4	5.1	3.8	2.7	2.2	1.7	1.4	1.1	0.97	0.79	0.68	0.60	0.53

[a] The zero-field units are 10^{-7} Ω cm; the linear terms are in units of 10^{-7} Ω cm/G; and the quadratic terms are in units of 10^{-9} Ω cm/G².

From these values for θ and α, the orientation in the laboratory frame of the binary direction and the line connecting the transverse contacts is obtained. Figure 4 is an example of the angular data from which this information was extracted. By orienting B such that $\theta-\alpha=0$, still maintaining $B_3=0$, A_{41} is obtained directly from $V_{T,\mathrm{Trig}}$ (Fig. 5). Then B may be oriented such that $\theta-\alpha=\frac{1}{2}\pi$. The linear contribution to $V_{T,\mathrm{Trig}}$ then gives $\rho_{23,1}$, the large Hall term, directly. Now with B again set so that $\theta-\alpha=0$, the variation of $V_{T,\mathrm{Trig}}$ with B_3, in principle, gives A_{44} directly. In practice, since A_{44} is a small term, measurements were also made with B reversed in sign so as to eliminate the (large) quadratic contribution. This procedure also corrects for the effect of any longitudinal offset of the transverse contacts [Eq. (11)], which is entirely quadratic in magnetic field.

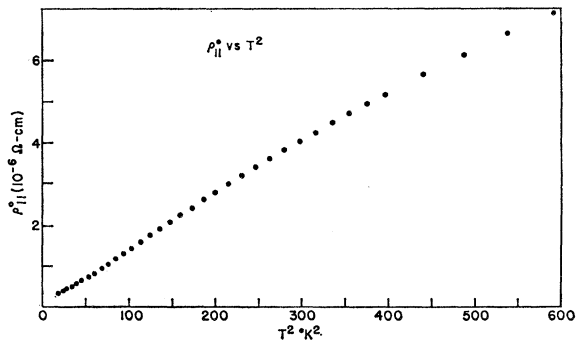

FIG. 6. Zero-field resistivity ρ_{11}^0 versus T^2.

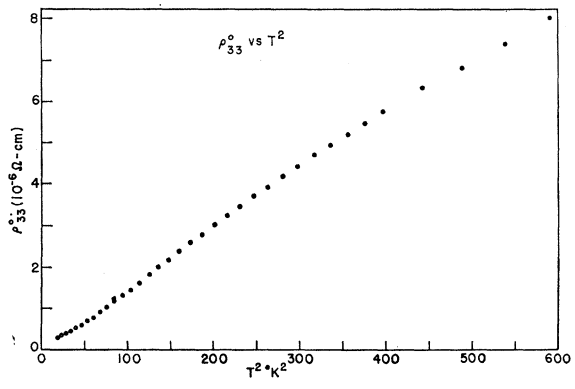

FIG. 7. Zero-field resistivity ρ_{33}^0 versus T^2.

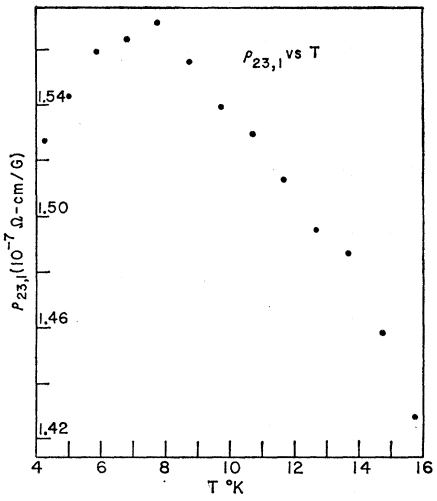

FIG. 8. Large Hall voltage $\rho_{23,1}$ versus the temperature.

From measurements of $V_{L,\text{Trig}}$ [Eq. (11)] one obtains A_{31}, A_{33}, and $\rho_{33}{}^0$ in an obvious way. For the binary sample, the measurement of α is difficult, but fortunately is unnecessary. It is only necessary to find the direction of the bisectrix axis, which corresponds to $\theta=0$ in the binary crystal. This is obtained by a procedure[27] that allowed the direction of the bisectrix axis to be located within 0.2°. It is clear from Eq. (12) that once the orientation of the bisectrix direction is established, the coefficient $\rho_{11}{}^0$, A_{11}, A_{12}, A_{13}, and A_{14} can be straightforwardly obtained. The remaining coefficient $\rho_{12,3}$ can be obtained from $V_{T,\text{Binary}}$ [Eq. (13)]. If α for this crystal were known (and it can in principle be obtained from $V_{T,\text{Binary}}$ by setting $B_1=0$, using the value of $\rho_{23,1}$ obtained from the trigonal crystal), then A_{14}, A_{44}, A_{11}, A_{12}, and A_{41} can be obtained redundantly.

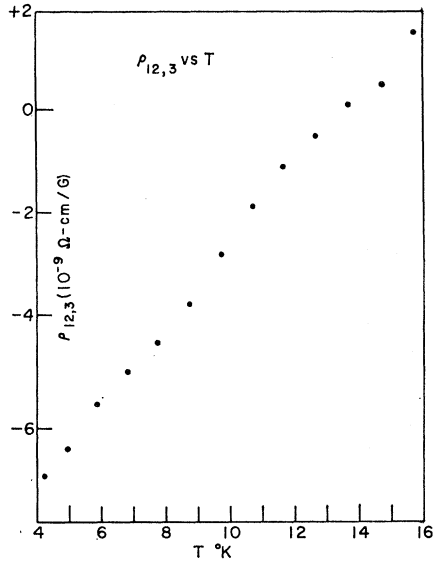

FIG. 9. Small Hall voltage $\rho_{12,3}$ versus the temperature.

[27] There is an empirically observed sharp minimum in the transverse magnetoresistance when B is near the bisectrix axis. For $B=105$ G, it is 1.8° from the bisectrix direction toward the trigonal [R. D. Brown (private communication)].

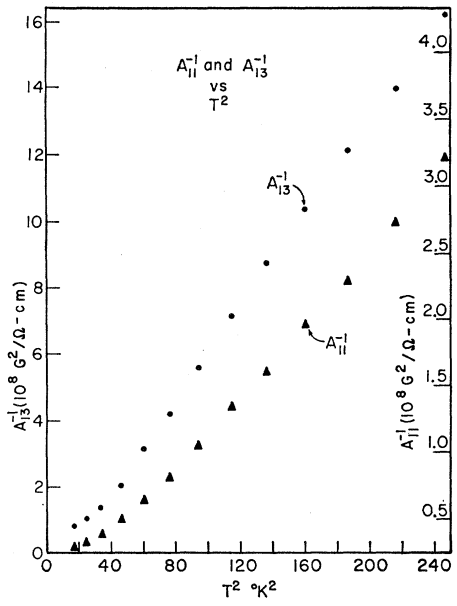

FIG. 10. Measured magnetoresistance ($A_{11}{}^{-1}$ and $A_{13}{}^{-1}$). The inverse magnetoresistances are plotted against the temperature squared in order to exhibit the T^{-2} dependence.

V. RESULTS

A. Experimental Galvanomagnetic Coefficients

The values of the tensor coefficients from 4 to 16°K are shown in Table I and Figs. 6–13. To obtain these

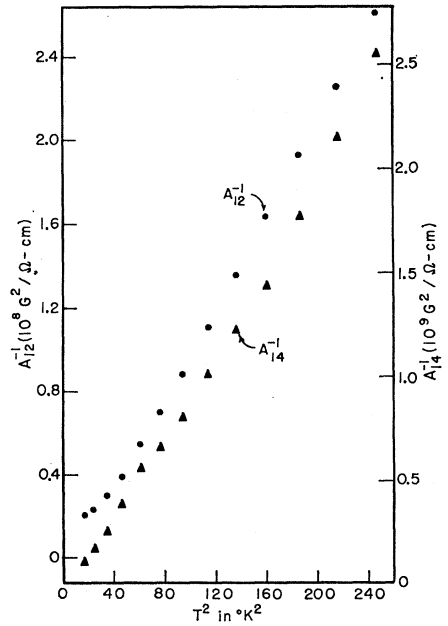

FIG. 11. The measured magnetoresistance ($A_{12}{}^{-1}$ and $A_{14}{}^{-1}$). The inverse magnetoresistances are plotted against the temperature squared in order to exhibit the T^{-2} dependence.

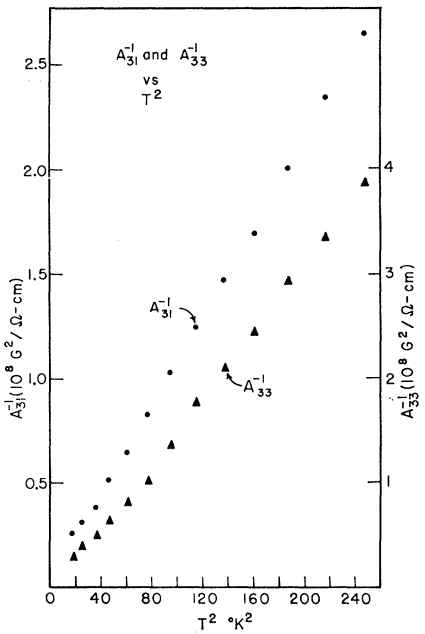

FIG. 12. The measured magnetoresistance (A_{31}^{-1} and A_{33}^{-1}). The inverse magnetoresistances are plotted against the temperature squared in order to exhibit the T^{-2} dependence.

values, the data for V_T and V_L [Eqs. (10)–(13)] for both samples, already in graphic form from the plotter, were transferred by a semiautomatic device to punched cards. An average of 40 points were taken per curve for approximately 1000 curves. All the algebraic operations necessary to extract the terms in V_L and V_T linear and quadratic in magnetic field were programmed for and performed on IBM 1620 and 7094 computers. These results were plotted versus either the magnetic field or

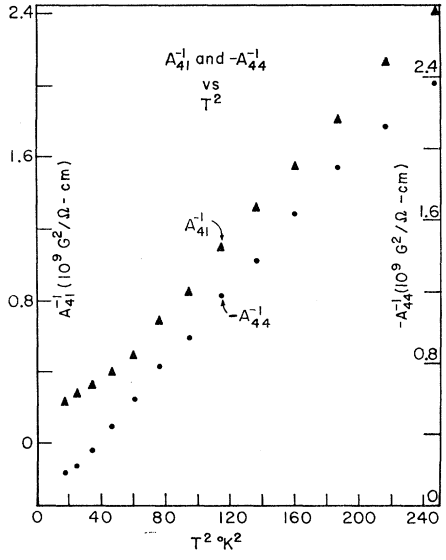

FIG. 13. Measured magnetoresistance (A_{41}^{-1} and A_{44}^{-1}). The inverse magnetoresistances are plotted against the temperature squared in order to exhibit the T^{-2} dependence.

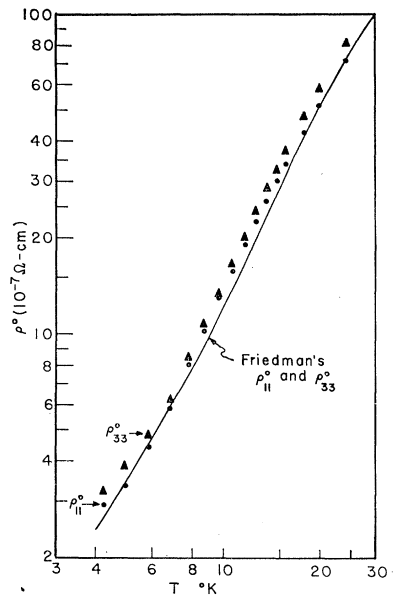

FIG. 14. Comparison of A. N. Friedman's curve for the zero-field resistance with our measured ρ_{11}^0 and ρ_{33}^0.

the magnetic field squared using an IBM 1627 graph plotter. The slope of the straight-line portion of one of these plots determined the value of a particular galvanomagnetic coefficient, and the region of linearity indicated the range of magnetic field over which the low-field condition was valid. The zero-field and quadratic magnetoresistance coefficients are plotted so as to show that the various components of mobility [cf. Eq. (B2)] vary as T^{-2} above $\sim$8°K.

The numerical value of the ratio of the 4.2°K resistance relative to the room-temperature resistance was different for the trigonal and binary samples. This difference, ideally, should be an indication of the variation of ρ_{11}^0/ρ_{33}^0 with temperature, but may well be due to differences in either impurity concentration or strain of the two samples. To settle this point, a separate experiment was performed using an "L"-shaped sample cut from the original crystal. ρ_{11}^0 and ρ_{33}^0 were both measured at 300°K, and then at 4.2°K. The ratio of the resistivity ratios ($R_{300}/R_{4.2}$) for the trigonal arm of the L to that for the binary arm was 1.20:1 compared to the ratio 1.27:1 for the trigonal and binary samples, indicating a small difference between the samples at the lowest temperatures.

The zero-field resistivity (Figs. 6 and 7) for which data were taken as high as 27°K agrees with the results of Friedman[5] (Fig. 14). The anisotropy in ρ_{11}^0 and ρ_{33}^0 is also indicated in Fig. 14. It should be noted that the relative values of either ρ_{11}^0 or ρ_{33}^0 are accurate to better than 1%, though there are larger errors ($\sim\pm5\%$) in their absolute values introduced by geometric factors. From 8–18°K, both ρ_{11}^0 and ρ_{33}^0 vary closely as T^2. Above $\sim$18°K the variation is somewhat less rapid. Below 8°K, ρ_{11}^0, and ρ_{33}^0 (and the inverse magneto-

resistivities) do not decrease as rapidly as T^2, but in this region, it is known[28] that the resistivity is sample-dependent, varying with impurity concentration and strain.

Table II gives the results of a least-squares fit to the data for the two zero-field and eight magnetoresistivity coefficients to the functions mT^2+b and $mT^{-2}+b$, respectively. The first two coefficients of the resistivity tensor are inversely proportional to mobility, and the last eight coefficients are directly proportional to mobility. The root-mean-squared error indicated a good fit because it was smaller than either the constant or the temperature-dependent contributions (in the temperature range 4–16°K). The temperature-dependent contribution was dominant in this temperature range. Since our model has, at most, eight variables, it is completely determined by any eight measured tensor coefficients. Therefore, the results in Table II already show that the larger mobilities vary as T^{-2} over the temperature range 7.78–15.7°K.

The experimental uncertainty of the relative values of $\rho_{23,1}$ is $\pm 1\%$, and $\pm 5\%$ for the absolute values, similar to the uncertainty of the field-independent terms. The variation of $\rho_{23,1}$ with T is slight, though there is a definite maximum near 8°K, in agreement with the observation of Friedman.[5] It should be noted that $|\rho_{12,3}|$ (Fig. 9) is about two orders of magnitude less than $|\rho_{23,1}|$, due to the almost complete cancellation of the Hall current contributions of the electrons and holes to $\rho_{12,3}$. The measured value for $\rho_{12,3}$ is then very sensitive to effects which may influence the electron and hole scattering differently. In the present case, the crystal was inadvertently strained before the $\rho_{12,3}$ data were taken, so that the numerical values of these data are not necessarily relevant to the unstrained crystal. There is no question, however, that $|\rho_{12,3}| \ll |\rho_{23,1}|$.

The estimated uncertainties in A_{11}, A_{12}, A_{13}, and A_{31}, the larger quadratic magnetoresistance coefficients, are less than 10% at the lower temperatures, and somewhat larger at the higher temperatures since the signals were smaller. To obtain larger signals the magnetic field strength was increased at the higher temperatures, maintaining $\mu B_{\max} \ll 1$. The sample current was also increased, while maintaining the condition that the self-magnetic field be $\sim 1\%$ of the smallest applied magnetic field. The accuracy did decrease nonetheless due to problems associated with temperature fluctuations and gradients. The uncertainty of the term A_{13} increased slightly more than the others as the temperature increased, since A_{13} is obtained from the difference of two measured quantities.

The estimated error in the smaller magnetoresistance coefficients A_{33}, A_{14}, A_{41}, and A_{44} was $\sim 15\%$, except for A_{14}. A_{14} was also obtained from the difference of two nearly equal quantities; the uncertainty ranged from $\pm 20\%$ at 4.2°K to $\pm 100\%$ at 16°K. None of the values for the various coefficients was obtained redundantly. The only other values for these coefficients in this temperature range are Zitter's measurements at 4.2°K, obtained from samples of lower purity. Table III shows a comparison of his results with the present data. In the last column his values are shown scaled to the present results, using a factor of 2.4 obtained from the relative residual resistivities of his sample and ours, applied to Eq. (B2). The results, within the combined experimental uncertainties, are in good agreement.

TABLE II. Measured zero-field resistivities and the magnetoresistivities fitted by least squares with $\rho=mT^2+b$ (from 4.23 to 15.7°K) and $A=mT^{-2}+b$ (from 7.78 to 15.7°K), respectively.

	m	b
	($10^{-7}\,\Omega\,\mathrm{cm/°K^2}$)	($10^{-7}\,\Omega\,\mathrm{cm}$)
ρ_{11}^0	0.139	−0.1
ρ_{33}^0	0.153	−0.5
	($10^{-7}\,\Omega\,\mathrm{cm°K^2/G^2}$)	($10^{-7}\,\Omega\,\mathrm{cm/G^2}$)
A_{11}	10.2	−0.01
A_{12}	11.6	−0.01
A_{13}	2.05	−0.003
A_{31}	9.3	+0
A_{33}	0.8	−0.0007
A_{14}	1.2	−0
A_{41}	1.3	−0.001
A_{44}	−1.0	+0

TABLE III. Comparison of the measured values of the resistivity tensor coefficients with those of Zitter at 4.2°K.

	Zitter	Present work	Zitter's values scaled[a]
ρ_{11}^0	7.4 ±5%	2.91±5%	3.08
ρ_{33}^0	8.0	3.21±5%	3.33
$\rho_{23,1}$	1.53±5%	1.54±5%	1.53
$\rho_{12,3}$	−0.25±8%	−0.07[a]	−0.25[a]
A_{11}	1.5 ±10%	3.5 ±8%	3.6
A_{12}	2.0	4.8 ±5%	4.8
A_{13}	0.45	1.2 ±10%	1.1
A_{31}	1.9	3.8 ±8%	4.5
A_{33}	0.16	3.3 ±10%	3.8
A_{14}	0.29±15%	0.93±20%	0.7
A_{41}	0.2	0.45±15%	0.48
A_{44}	−0.33±20%	−0.58±15%	−0.79

[a] See text.

B. Determination of Model Parameters

Table IV lists the parameters of the two-carrier model (i.e., three tilted electron ellipsoids and one hole ellipsoid of revolution) obtained for each temperature by computing the galvanomagnetic coefficients from the model and comparing them to the experimental values, using a least-squares criteria for judging the best fit. The predictions of the model using these parameters are compared with the data in Table I.

The model has eight parameters which must be varied to fit Eq. (B2) to the data. However, the value of $c=P/N$ has been measured as $1.0\pm 5\%$ by Brown[29] on

[28] A. N. Friedman and S. H. Koenig, IBM J. Res. Develop. 4, 158 (1960).

[29] R. D. Brown, III (private communication).

TABLE IV. The parameters of the two-carrier model, obtained by a least-squares fit to the galvanomagnetic data, versus temperature. Below are Zitter's[a] published values at 4.2°K. All tabulated values are in units of 10^6 cm²/V sec. $N=2.7\times10^{17}$ cm$^{-3}\pm8\%$; $C=P/N=1.0\pm5\%$.

Temperature (°K)	μ_1	μ_2	μ_3	μ_4	ν_1	ν_3
4.23	110	3	67	−7.1	22	3.5
4.94	98	2.7	56	−5.8	18	3.4
5.88	78	2	46	−4.7	13	2.8
6.82	58	1.4	35	−3.7	9.9	1.7
7.78	40	0.61	27	−2.9	8.1	1.4
8.74	32	0.45	21	−2.3	6.4	1.1
9.72	25	0.34	16	−1.8	5.2	0.91
10.7	21	0.24	13	−1.4	4.2	0.74
11.7	17	0.20	11	−1.16	3.6	0.63
12.7	14.6	0.16	9.1	−0.98	3.0	0.53
13.7	12.6	0.13	7.8	−0.84	2.6	0.47
14.7	10.7	0.11	6.6	−0.71	2.3	0.4
15.7	9.4	0.09	5.8	−0.63	2.0	0.35
Estimated error	8%	20%	5%	10%	10%	40%
Zitter's value at 4.2°K[a]	43	0.6	30	+3.4	12	1.0

[a] Zitter's estimated errors are ±10% except for the error in μ_2, which is ±20%, and ν_3, which is 100%.

TABLE VI. A least-squares fit of the mobilities to $mT^{-2}+b$ over the temperature range 7.78–15.7°K.

	m (10^8 cm² °K²/V sec)	b (10^8 cm²/V sec)	rms error
μ_1	+25.0	−0.009	0.002
μ_2	+0.41	−0.0009	0.0001
μ_3	+16.9	−0.01	0.002
μ_4	−1.83	+0.001	0.0002
ν_1	4.9	−0.0001	0.0003
ν_3	0.84	+0.0001	5×10^{-5}

samples cut from the crystal used in the present experiment, an accuracy equal to or greater than the results of the present work. Therefore, in fitting the data, c was constrained to equal 1.0.

It was convenient to have a set of approximate expressions relating the coefficients of the resistivity tensor and the mobilities. These relations, first derived by Zitter, are given in Appendix D in our notation and are far simpler than the exact equations. They are useful in indicating how the components of the resistivity tensor vary as the dominating mobility components change. A first fit was attempted in which all terms were weighted according to their estimated experimental random uncertainties, but not allowing for systematic errors.

The fit, though informative, gave physically unreasonable values for the smaller model parameters (e.g., negative values for an intrinsically positive mobility term). The major problem appeared to be associated with $\rho_{12,3}$. Though the data (Fig. 9), appear to have little random scattering, there may well be a large systematic error in the results due to the fact, mentioned earlier, that the results were obtained after the sample had become strained. To obtain a realistic fit, $\rho_{12,3}$ was effectively excluded from the fitting procedure by using a weight factor of 10^{-3} compared to weight factors on the order of 10 for most of the other terms. It is unfortunate that the data for $\rho_{12,3}$ cannot be used here, since as Table V shows, $\rho_{12,3}$ is very sensitive to changes in μ_1, μ_2, and ν_1. The agreement of the values predicted by the set of model parameters with the experimental values (Table I) for $\rho_{11}{}^0$, $\rho_{33}{}^0$, $\rho_{23,1}$, A_{11}, and A_{12} is excellent; of the order of a few percent for most temperatures. The differences between the predicted and measured values of A_{13}, A_{33}, and A_{41} are within experimental error over the entire temperature range. The agreement of the predictions with the experimental results are poorest for A_{31} and A_{44}, both relatively difficult to measure. The disagreement, however, is not so severe as to suggest any inadequacy of the model.

The differences between the measured and predicted values for A_{14} was within the estimated experimental uncertainty of 20% at 4.2°K, increasing to 100% at 15.7°K. Since the error was so large this term did not significantly effect the final values of the model parameters. However, the measured and predicted values of A_{14} agreed in sign with A_{41} thereby fixing the sign μ_4, the off-diagonal electron mobility, as negative. Figures 15–18 show that all the calculated mobilities vary

TABLE V. Percentage variation in the absolute value of the tensor coefficients as the mobilities and P/N are increased and decreased 10% about the values that produced a best fit at 4.2°K.[a]

	μ_1		μ_2		μ_3		μ_4		ν_1		ν_3		$C=P/N$	
	+10%	−10%	+10%	−10%	+10%	−10%	+10%	−10%	+10%	−10%	+10%	−10%	+10%	−10%
$\rho_{11}{}^0$	−6.5	+7.5	−0.19	+0.19	0	0	0	0	−2.7	+2.9	0	0	−2.7	+2.9
$\rho_{33}{}^0$	0	0	0	0	−8.7	+10.5	0	0	0	0	−0.5	+0.5	−0.5	+0.5
$\rho_{23,1}$	+2.8	−3.2	−0.08	−0.08	+0.7	−0.9	−0.14	+0.13	−2.9	+3.1	−0.7	+0.71	−3.4	+3.6
$\rho_{12,3}$	−31.4	+40.4	+21.7	+21.9	0	0	0	0	+57.1	−57.4	0	0	+24.4	−27.4
A_{11}	+5.9	−6.5	−0.9	+0.93	−9.7	−9.7	+0.73	−0.66	−5.4	+5.8	0	0	−5.4	+5.8
A_{12}	+5.0	−5.5	−0.77	+0.77	+8.2	−8.2	+0.33	−0.3	−4.5	+4.8	+1.6	−1.6	−3.8	+4.1
A_{13}	−0.7	+1.0	+6.6	−6.7	0	0	0	0	+4.5	−3.8	0	0	−2.6	+2.5
A_{31}	+2.7	−3.1	+0.08	−0.08	−0.02	+0.02	+0.06	−0.05	+6.9	−7.2	−0.01	+0.01	+5.8	−6.3
A_{33}	+10	−10	0	0	−16.6	+22.1	+21	−19	0	0	−0.99	+1.0	−0.99	+1.0
A_{14}	+5.9	−6.6	−0.66	+0.66	0	0	+10	−10	−5.4	+5.8	0	0	−5.4	+5.8
A_{41}	+3.0	−3.4	−0.47	+0.47	+0.4	−0.5	+10.2	−10.1	−2.7	+2.9	−0.5	+0.5	−3.2	+3.4
A_{44}	−4.1	+4.3	+1.96	−1.97	+0.01	−0.02	−0.03	+0.03	+12.2	−12.2	0	0	+3.5	−4.2

[a] All numbers in the table are precent. The + sign indicates an increase in absolute value, the − sign a decrease.

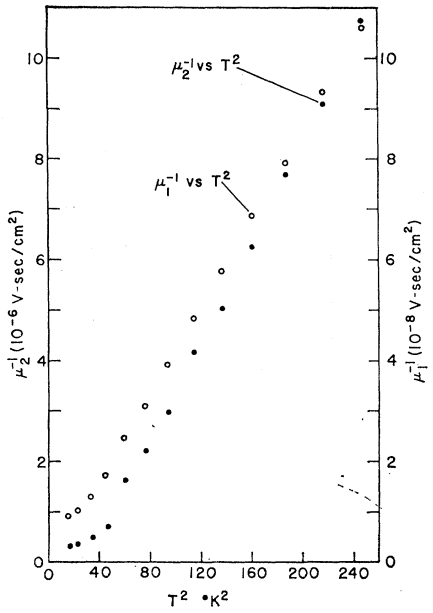

FIG. 15. Calculated electron mobilities (μ_1^{-1} and μ_2^{-1}). The inverse mobilities are plotted against the temperature squared in order to exhibit the T^{-2} dependence.

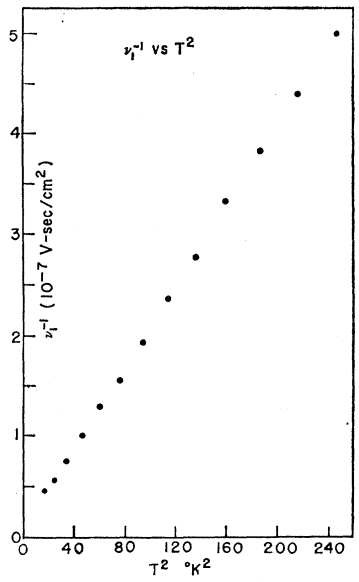

FIG. 17. Calculated hole mobility (ν_1^{-1}). The inverse mobilities are plotted against the temperature squared in order to exhibit the T^{-2} dependence.

closely as T^{-2} between 8 and 16°K. Table VI is a least-squares fit of the mobilities to $mT^{-2}+b$, where b may be thought of as mainly due to residual resistance. For $T\simeq 10$°K, it is clear from this table that the residual resistance contribution is unimportant.

The estimated uncertainties for the various model parameters are given at the bottom of Table V. These values are really judgments, obtained by computing the predicted values of the galvanomagnetic coefficients as the model parameters were varied about their least-squares values. These results were then compared with the experimental results and associated experimental uncertainty. With the exception of μ_2 and ν_3, which are very low mobilities, the parameters of the model are known within 10%. The larger errors associated with μ_2 and ν_3 (coming mainly from the uncertainty in A_{13} for μ_2, and A_{12} and A_{33} for ν_3) do not appear as scatter in Figs. 15 and 18, for reasons which are not entirely clear. The presumption is, however, that though the

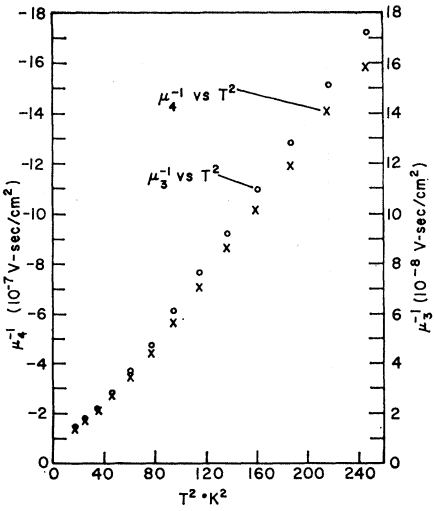

FIG. 16. Calculated electron mobilities (μ_3^{-1} and μ_4^{-1}). The inverse mobilities are plotted against the temperature squared in order to exhibit the T^{-2} dependence.

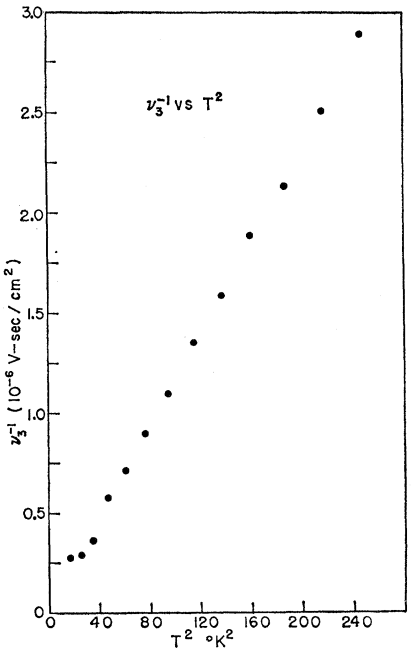

FIG. 18. Calculated hole mobility (ν_3^{-1}). The inverse mobilities are plotted against the temperature squared in order to exhibit the T^{-2} dependence.

variation of both μ_2 and ν_3 with T is smooth, there are systematic errors in the absolute magnitude of the curves.

As pointed out in Sec. II, there are identities that the measured coefficients of the resistivity tensor must satisfy because the model used for the Fermi surface has fewer parameters than the number of measureable coefficients. Equations (6) and (7) are two of these, expressed in terms of coefficients of the conductivity tensor (Appendix C). In addition, the inequality in Eq. (8) must be satisfied by the data. To use the identity tests [cf. Eqs. (6) and (7)], the dependence of the identities on $\rho_{12,3}$ must be examined since $\rho_{12,3}$ is not accurately known. In Eq. (6), $\rho_{12,3}$ enters only as part of S_{44}, a very small term compared to S_{11}. Two sides of Eq. (6) were compared at each temperature using both the measured and predicted values of $\rho_{12,3}$ listed in Table I. For all the values of $\rho_{12,3}$ used, the first identity was well satisfied; i.e., with the exception of three values of $\rho_{12,3}$ used, both sides of Eq. (6) were equal within $\pm 3\%$, an amount far smaller than expected considering the estimated experimental uncertainties in the measured quantities.

The other identity [Eq. (7)] is more complicated. $\rho_{12,3}$ enters both sides in the form of a ratio and a sum. Since it contributes approximately the same amount to both sides, the identity may be satisfied even though the values of $\rho_{12,3}$ are in error. This was found to be the case; the two sides of Eq. (7) were equal within the estimated experimental uncertainties.

The model predicts that the conductivity component S_{44} will be negative. S_{44} was calculated from the measured coefficients of the resistivity tensor (cf. Appendix C) and was negative, using either the predicted or measured values of $\rho_{12,3}$. The magnitude of S_{44} was at least six times the uncertainty.

The values of the model parameters can be compared to the results of Zitter[6] and Friedman.[5] Friedman was able to estimate the values of μ_1 and ν_1 (cf. Table IV) from measurements of the zero-field resistances and the Hall term $\rho_{23,1}$, using the approximate equations (see Appendix D). The agreement between Friedman's and our μ_1 and ν_1 is excellent. Furthermore, Friedman's curves for μ_1 and ν_1 have the same T^{-2} dependency observed here. Zitter's values for the model parameters were obtained from data taken on samples at a temperature (4.2°K) at which impurity scattering was dominant. All his mobilities are in good agreement with ours using the same scale factor of 2.4 that was applied to his resistivities, except μ_2 and ν_1.

VI. DISCUSSION OF RESULTS

Two fundamentally different sets of information about bismuth are provided by the results. The values of the model parameters at any one temperature provide information about the band structure of bismuth, while their temperature variation gives information about the scattering mechanisms that determine electrical transport. Our results concerning the band structure are mainly corroborative. On the other hand, the major transport result, i.e., that the components of the mobility tensors vary as T^{-2}, indicates that the dominant scattering mechanism in bismuth is different from the T^{-1} dependence that one anticipates for deformation potential scattering.[8] We will discuss these points separately.

A. Band Structure with the Relaxation Approximation

As has been seen, the transport data at any temperature is consistent with the generally accepted band model for bismuth. The total electron carrier density determined in this experiment is $N=2.7\pm0.2\times10^{17}$ cm^{-3}. Bhargava[2] has reported the values $n=0.96\pm0.05\times10^{17}$ cm^{-3} for the carrier density per electron ellipsoid and $p=3.0\pm0.1\times10^{17}$ cm^{-3} for the hole ellipsoid, both obtained from de Haas–van Alphen data. Williams[30] has reported $3n=p$, or $N=P\simeq3.1\pm0.1$ cm^{-3}, from Alfvén-wave propagation. The experimental uncertainty in our value of N is that associated with fitting the data to the (generally accepted) two-band model. The agreement of this N with the de Haas–van Alphen value is good. The question may be asked, however, in what way a more complex model might alter N. The possibility of a third band near the Fermi surface has been discussed.[31,32] If such a band were present and contributed carriers in the temperature range of our measurements, the equation for $\rho_{23,1}$, Appendix D, would become

$$\rho_{23,1}\simeq[Ne(1+2c\nu_1/\mu_1+c'\mu_0/\mu_1)]^{-1}, \qquad (14)$$

where c' and μ_0 are parameters, analogous to c and ν_1, that would describe these carriers. If these carriers were electrons, the net results would be to *decrease* the predicted value for N, reducing the agreement with the de Haas–van Alphen and Alfvén-wave results. If they were holes, the new term would be included in the term $2c\nu_1/\mu_1$, since the data reduction procedure set $c=1$. This would not affect N, but would alter the value ν_1, an effect which would not be recognized, since ν_1 is not known *a priori*.

The electron mobility tensor for each temperature was diagonalized (cf. Table VII) yielding components (labeled μ_1^*, μ_2^*, μ_3^*). The electron mobility anisotropy ratios $1:\mu_2^*/\mu_1^*:\mu_3^*/\mu_1^*$ and the mobility tilt angle θ_μ [calculated from Eq. (4)] for each temperature are also tabulated in Table VII. The hole mobilities are also in Table VII.

Within the spirit of the relaxation-time approximation, the relative values of the components of the carrier mobility tensors can be related to the components of the relevant mass tensors. Equation (1), on which the

[30] G. A. Williams, Phys. Rev. **139**, A771 (1965).
[31] R. D. Brown, III, Bull. Am. Phys. Soc. **13**, 44 (1957).
[32] A. A. Lopez, Phys. Rev. **175**, 823 (1968).

entire analysis of the data is based, assumes that a relaxation tensor can be defined from which the zero-field conductivity, the linear Hall effect, and the quadratic magnetoresistance can be computed in a consistent manner. Basic to this is the assumption that the presence of the magnetic field does not effect the term in the expansion of the momentum distribution function linear in the applied electric field. The range of validity of the relaxation-time approximation for anisotropic bands has been discussed by Herring and Vogt[15]; Price[33] has extended these considerations to include the effect of the presence of a magnetic field.

The fact that the tilt angle θ_μ for the mobility tensor (Table VII) agrees very well with the tilt angle of 6.4° for the surfaces of constant electron energy[2,4] shows that if a relaxation-time tensor $\boldsymbol{\tau}$ is defined, such that $\boldsymbol{\mu}=e\boldsymbol{\alpha}\cdot\boldsymbol{\tau}$, both $\boldsymbol{\tau}$ and $\boldsymbol{\alpha}$ would have the same principal axis. For this case the components of $\boldsymbol{\alpha}$ can be easily obtained from the cyclotron masses; the result is $1:\alpha_2^*/\alpha_1^*:\alpha_3^*/\alpha_1^*=1.0:0.004:0.62$, using Kao's[34] cyclotron masses. The values for the tensor components of $\boldsymbol{\tau}$ are tabulated in Table VIII. The anisotropy of $\boldsymbol{\tau}_e$ is seen to vary from ~5:1 at 4.2°K to roughly isotropic at 16°K; the anisotropy of τ_h is 2:1 over the entire range of temperature. Herring and Vogt[15] argue (cf. their Table IX) that for a scattering anisotropy in two orthogonal directions ~5:1 or less, the collision integral can be well approximated by a tensor relaxation time. This point, plus the fact that a single $\boldsymbol{\tau}$ allows one to fit all the data using a simple band-structure model and the formulas [Eqs. (6)–(8) and Appendix B] derived using Eq. (1), give a self-consistent argument for the reasonableness of working within the relaxation-time approximation.

In total, we find nothing inconsistent with assuming the two-band model for bismuth and a tensor relaxation time for each type of carrier that is an order of magnitude less anisotropic than the associated mass tensor and that has the same principal axes as the mass tensor.

TABLE VII. Electron mobilities in the principal-axis system of the electron ellipsoid in units of 10^6 cm²/V sec, together with the ratio of the mobilities, the mobility, the tilt angle, and the values of ν_1/μ_1.

	μ_1^*	μ_2^*	μ_3^*	$\mu_1^*:\mu_2^*:\mu_3^*$	θ_μ	ν_1/μ_1
4.23	110	2.2	67.8	1:0.020:0.62	6.3	0.200
4.94	98	2.1	56.1	1:0.021:0.57	6.2	0.183
5.88	77.8	1.5	46.2	1:0.020:0.59	6.1	0.171
6.82	58.3	1.0	35.5	1:0.017:0.61	6.1	0.170
7.78	40.4	0.3	27.1	1:0.007:0.67	6.3	0.201
8.74	32.2	0.2	21.2	1:0.006:0.66	6.2	0.198
9.72	25.4	0.1	16.5	1:0.006:0.65	6.2	0.204
10.7	20.6	0.08	13.2	1:0.004:0.64	6.3	0.205
11.7	17.3	0.07	11	1:0.004:0.63	6.1	0.208
12.7	14.6	0.05	9.2	1:0.004:0.63	6.1	0.206
13.7	12.6	0.04	7.9	1:0.003:0.63	6.1	0.206
14.7	10.7	0.03	6.7	1:0.003:0.62	6.1	0.212
15.7	9.4	0.02	5.9	1:0.003:0.62	6.3	0.212

[33] P. J. Price, IBM J. Res. Develop. **1**, 239 (1957).
[34] Y. H. Kao, Phys. Rev. **129**, 1122 (1963).

TABLE VIII. Relaxation time for the electrons (in the principal axis of the electron ellipsoid) and the holes as a function of temperature in units of 10^{-10} sec.

	Electrons			Holes	
	τ_{1e}	τ_{2e}	τ_{3e}	τ_{1h}	τ_{3h}
4.23	4.4	21.6	4.4	8.5	15
4.94	3.9	20.3	3.7	6.9	15
5.88	3.1	14.7	3.0	5.1	12
6.82	2.3	9.9	2.3	3.8	7.4
7.78	1.6	2.8	1.8	3.1	6.0
8.74	1.3	2.0	1.4	2.5	4.8
9.72	1.0	1.4	1.1	2.0	3.9
10.7	0.83	0.82	0.86	1.6	3.2
11.7	0.70	0.72	0.72	1.4	2.7
12.7	0.59	0.52	0.60	1.2	2.3
13.7	0.51	0.38	0.52	1.0	2.0
14.7	0.43	0.32	0.44	0.87	1.7
15.7	0.38	0.24	0.38	0.77	1.5

In relation to the above, there are two fine points to be mentioned. First, Table VII lists the magnitude of the tilt angle. The question of the sign is more subtle. This has been discussed in detail in a recent publication,[4] in which it is shown that the signs of θ_μ and θ_α are the same (and positive).

The second point involves possible corrections to the data because of boundary scattering (size effects). From the values for $\boldsymbol{\tau}$, the band parameters, and the Fermi energy, one can obtain values for the carrier mean free path in different principal directions. At 4.2°K, they are

$$\begin{array}{ccccc} l_{1e}^*, & l_{2e}^*, & l_{3e}^*, & l_{1h}^*, & l_{3h}^*, \\ 0.39\,\text{mm} & 0.12\,\text{mm} & 0.30\,\text{mm} & 0.23\,\text{mm} & 0.11\,\text{mm}. \end{array} \quad (15)$$

These decrease quadratically as the temperature increases. The largest mean-free-path component is ~5% of the sample diameter, and then only at the lowest temperature. The size effect correction to the conductivity using either the experimental results [Friedman and Koenig,[28] Figs. 2(a) and 2(b)] or the theoretical results [Price,[35] Eq. (22)] for the influence of sample size on conductivity, is negligible.

B. Carrier Scattering Mechanism

The de Broglie wavelength of the carriers in bismuth, both for electrons and holes, is very long: hundreds of times the lattice parameter. Thus, the carriers see the lattice as a continuum, and their interaction with phonons, expressible by a deformation potential,[8] is via the long-wavelength strain in the lattice that the phonons produce. Mase *et al.* have computed the deformation-potential tensor components necessary to describe their galvanomagnetic data at 20.4°K. The results (1) are somewhat larger than that expected from strain measurements and (2) do not consider any screening of the deformation potential interaction by the carriers, which would require that the actual

[35] P. J. Price, IBM J. Res. Develop. **4**, 152 (1960).

deformation-potential tensor components be much larger than the values they derived. Considering these two points, and the fact that the deformation potential enters quadratically into the scattering, we feel that this model is inadequate to explain the conductivity in bismuth. More significantly, the temperature dependence of the conductivity predicted by the deformation-potential model disagrees with our observations.

We propose that the predominant carrier scattering mechanism in bismuth, when the mobility varies as T^{-2}, is a particular type of carrier-carrier interaction in which two carriers in separate valleys scatter, but remain in their respective valleys conserving energy and momentum in their c.m. system. Baber[36] discussed scattering of this sort between electrons and holes in different bands, and pointed out that for this case, conservation of momentum is not equivalent to conservation of current, and that therefore this type of scattering contributes to the resistivity. There is no contribution to the resistivity, however, if the two carriers are of the same sign and have isotropic masses. For carriers with an anisotropic mass, collisions which conserve the momentum of the distribution may not conserve the total current. This situation has been previously discussed with regard to the temperature-dependent part of the residual resistance of degenerate n-type germanium.[37] In either the electron-hole or the anisotropic-carrier case, the temperature dependence is as T^{-2}. For bismuth, we believe that essentially all the scattering is this type of carrier-carrier scattering.

One may readily estimate the magnitude of the scattering from the known scattering of carriers by ionized impurities, since a similar screened Coulomb potential is involved. From the considerations of Katz *et al.*,[37] one expects the mobility to be given by

$$\mu=\mu_i(n_i/n)(T_D/T)^2, \tag{16}$$

where μ_i is the mobility for bismuth with n_i singly ionized impurities, and $n=3\times10^{17}$ cm^{-3}. Substituting Bhargava's[2] values of μ_i for electrons and holes for his alloy No. 5, with $n_i\approx10^{17}$ cm^{-3} and $T_D\sim130$°K, we obtain $\mu_e=9\times10^7$ cm^2/V sec, $\mu_h=6\times10^6$ cm^2/V sec, in good agreement with our results (cf. Table IV).

C. T Dependence of $\rho_{23,1}$

From Fig. 10, one sees that to first order $\rho_{23,1}$, which essentially measures N, is independent of temperature. However, there is a small but measureable variation of $\rho_{23,1}$ with temperature that has also been reported by Friedman.[5] This temperature variation, with a maximum at ~7°K, has two causes. From the expression for $\rho_{23,1}$, Appendix D, it is seen that a temperature dependence of both N and the ratio ν_1/μ_1 can contribute. Below ~10°K, the variation of N as computed from the Fermi function is negligible and the variation of $\rho_{23,1}$ follows from the variation of ν_1/μ_1 listed in Table VII. Above ~10°K the temperature variation of N is the predominant factor, both as seen from Table VII and as expected from the fact that all mobilities are varying as T^{-2} and, therefore, the ratio ν_1/μ_1 does not vary. On the other hand, below ~8°K, the T^{-2} law breaks down first for μ_1 and then for ν_1 (cf. Figs. 15 and 17), which explains empirically the maximum in $\rho_{23,1}$. The deviation from the T^{-2} law is due to scattering by residual impurities, as is clear *a priori* from the results of Friedman,[5] though it is not clear why the effect should necessarily be greater for electrons than holes.

[36] W. G. Baber, Proc. Roy. Soc. (London) **A158**, 383 (1937).
[37] M. Katz, S. H. Koenig, and A. A. Lopez, Phys. Rev. Letters **15**, 828 (1965).

VII. CONCLUSIONS

Within the framework of the accepted band structure of bismuth, the electron and hole mobilities and the carrier concentration have been obtained by a least-squares fit to the galvanomagnetic coefficients, measured to order H^2, in the temperature range 4–16°K. The carrier concentration N and the mobility tilt angle are constant over the entire temperature range, with $N=2.7\times10^{17}$ cm$^{-3}\pm8\%$ and $\theta_\mu=6.2°$, respectively. The agreement between the mobility tilt angle and the effective-mass tilt angle demonstrates that the principal axes of the two tensors are coincident within the experimental uncertainty. We find that the accepted band structure is fully consistent with all our results.

One of the most significant results of this experiment is that all the components of the mobility tensors for both the electrons and holes vary as T^{-2} in the range 8–16°K. We argue that the scattering is between carriers in different valleys. The magnitude of this scattering was estimated from Bhargava's data for ionized impurity scattering in bismuth. The mobilities calculated from these cross sections were in agreement with the measured mobilities. Bismuth is unique in that the main carrier scattering mechanism is unlike that which dominates the scattering in any other material.

ACKNOWLEDGMENTS

The author would like to thank Dr. Seymour H. Koenig for suggesting the present investigation and for his continued guidance and encouragement throughout the work; Dr. Peter Price for numerous enlightening discussions; Dr. Alberto Lopez, Dr. Rameshwar Bhargava, Dr. Joseph Krieger, Walter Schillinger, and Rodney D. Brown for helpful stimulating discussions; Dr. R. L. Garwin for suggesting the use of the VMM program; Dr. Andrew Kotchoubey for his assistance with the VMM programming; Dr. A. Segmuller and J. Angilello, who took the Laue photographs. Many other members of the Watson staff were also of invaluable assistance, especially the staff of the model shop under the direction of John Sierssen, and the staff of the electronics shop under the direction of Joseph Cozzo; Mrs. Alice Kelbl drew the figures, and Mrs. Rita St. Marie and Miss Nancy Kaliczer graciously typed the manuscript.

APPENDIX A: EXPANSIONS FOR THE CONDUCTIVITY TENSOR $\sigma(B)$ AND RESISTIVITY TENSOR $\varrho(B)$

$$\boldsymbol{\sigma}(\mathbf{B})=\begin{pmatrix}\sigma_{11}^0 & 0 & 0\\ 0 & \sigma_{11}^0 & 0\\ 0 & 0 & \sigma_{33}^0\end{pmatrix}-\begin{pmatrix}0 & \sigma_{12,3}B_3 & -\sigma_{23,1}B_2\\ -\sigma_{12,3}B_3 & 0 & \sigma_{23,1}B_1\\ \sigma_{23,1}B_2 & -\sigma_{23,1}B_1 & 0\end{pmatrix}$$
$$-\begin{pmatrix}S_{11} & S_{12} & S_{13} & S_{14} & 0 & 0\\ S_{12} & S_{11} & S_{13} & -S_{14} & 0 & 0\\ S_{31} & S_{31} & S_{33} & 0 & 0 & 0\\ S_{41} & -S_{41} & 0 & S_{44} & 0 & 0\\ 0 & 0 & 0 & 0 & S_{44} & S_{41}\\ 0 & 0 & 0 & 0 & S_{14} & \frac{1}{2}(S_{11}-S_{12})\end{pmatrix}\begin{pmatrix}B_1^2\\ B_2^2\\ B_3^2\\ 2B_2B_3\\ 2B_3B_1\\ 2B_1B_2\end{pmatrix}, \tag{A1}$$

$$\boldsymbol{\varrho}(\mathbf{B})=\begin{pmatrix}\rho_{11}^0 & 0 & 0\\ 0 & \rho_{11}^0 & 0\\ 0 & 0 & \rho_{33}^0\end{pmatrix}+\begin{pmatrix}0 & \rho_{12,3}B_3 & -\rho_{23,1}B_2\\ -\rho_{12,3}B_3 & 0 & \rho_{23,1}B_1\\ \rho_{23,1}B_2 & -\rho_{23,1}B_1 & 0\end{pmatrix}$$
$$+\begin{pmatrix}A_{11} & A_{12} & A_{13} & A_{14} & 0 & 0\\ A_{12} & A_{11} & A_{13} & -A_{14} & 0 & 0\\ A_{31} & A_{31} & A_{33} & 0 & 0 & 0\\ A_{41} & -A_{41} & 0 & A_{44} & 0 & 0\\ 0 & 0 & 0 & 0 & A_{44} & A_{41}\\ 0 & 0 & 0 & 0 & A_{14} & \frac{1}{2}(A_{11}-A_{12})\end{pmatrix}\begin{pmatrix}B_1^2\\ B_2^2\\ B_3^2\\ 2B_2B_3\\ 2B_3B_1\\ 2B_1B_2\end{pmatrix}. \tag{A2}$$

APPENDIX B: TENSOR COMPONENTS

1. Conductivity Tensor Components as Functions of the Mobilities N and P

($N=3n$, where n is the number of electrons per ellipsoid, P is the total number of holes in the hole ellipsoid, and $e=|e|$.)

$$\begin{aligned}
&\sigma_{11}^0=(\tfrac{1}{2}Ne)(\mu_1+\mu_2)+Pe\nu_1,\quad \sigma_{33}^0=Ne\mu_3+Pe\nu_3,\\
&\sigma_{12,3}=Ne\mu_1\mu_2-Pe\nu_1^2,\quad \sigma_{23,1}=(\tfrac{1}{2}Ne)[(\mu_1+\mu_2)\mu_3-\mu_4^2]-Pe\nu_1\nu_3,\\
&S_{11}=(\tfrac{1}{8}Ne)[(\mu_1-\mu_2)^2\mu_3+(5\mu_1-\mu_2)\mu_4^2],\quad S_{12}=(\tfrac{1}{8}Ne)[(3\mu_1^2+3\mu_2^2+2\mu_1\mu_2)\mu_3-(\mu_1+3\mu_2)\mu_4^2]+Pe\nu_1^2\nu_3,\\
&S_{13}=(\tfrac{1}{2}Ne)[\mu_1\mu_2(\mu_1+\mu_2)]+Pe\nu_1^3,\quad S_{31}=(\tfrac{1}{2}Ne)[(\mu_1+\mu_2)\mu_3^2-\mu_3\mu_4^2]+Pe\nu_1\nu_3^2,\\
&S_{33}=Ne\mu_1\mu_4^2,\quad S_{14}=-(\tfrac{1}{4}Ne)\mu_4\mu_1(\mu_1-\mu_2),\\
&S_{41}=-(\tfrac{1}{4}Ne)\mu_4[\mu_3(\mu_1-\mu_2)+\mu_4^2],\quad S_{44}=-[(\tfrac{1}{4}Ne)\mu_1\mu_2\mu_3+(\tfrac{1}{2}Pe)\nu_1^2\nu_3].
\end{aligned} \tag{B1}$$

2. Resistivity Tensor Components as Functions of the Mobilities N and P

[Here $c=P/N$ should not be confused with c used for the speed of light in, e.g., Eq. (4).]

$$\begin{aligned}
&\rho_{11}^0=(2/Ne)(\mu_1+\mu_2+2c\nu_1)^{-1},\quad \rho_{33}^0=(1/Ne)(\mu_3+c\nu_3)^{-1},\\
&\rho_{12,3}=(4/Ne)(\mu_1\mu_2-c\nu_1^2)(\mu_1+\mu_2+2c\nu_1)^{-2},\quad \rho_{23,1}=(1/Ne)[\mu_3(\mu_1+\mu_2)-2c\nu_1\nu_3-\mu_4^2](\mu_1+\mu_2+2c\nu_1)^{-1}(\mu_3+c\nu_3)^{-1},\\
&A_{11}=(1/2Ne)[\mu_3(\mu_1-\mu_2)^2+\mu_4^2(5\mu_1-\mu_2)](\mu_1+\mu_2+2c\nu_1)^{-2},\\
&A_{12}=(1/2Ne)\{\mu_1(3\mu_1\mu_3+\mu_4^2)+(2\mu_1+3\mu_2)(\mu_2\mu_3-\mu_4^2)+8c\nu_1^2\nu_3\\
&\qquad -2[(\mu_1+\mu_2)\mu_3-2c\nu_1\nu_3-\mu_4^2]^2(\mu_3+c\nu_3)^{-1}\}(\mu_1+\mu_2+2c\nu_1)^{-2},\\
&A_{13}=(2/Ne)[\mu_1\mu_2(\mu_1+\mu_2)+2c\nu_1^3-4(\mu_1\mu_2-c\nu_1^2)^2(\mu_1+\mu_2+2c\nu_1)^{-1}](\mu_1+\mu_2+2c\nu_1)^{-2},\\
&A_{31}=(1/2Ne)\{2c\nu_1(\mu_1+\mu_2)(\mu_3+\nu_3)^2+\mu_4^2[\mu_3(\mu_1+\mu_2)-\mu_4^2-2c\nu_1(\mu_3+2\nu_3)]\}(\mu_1+\mu_2+2c\nu_1)^{-1}(\mu_3+c\nu_3)^{-2},\\
&A_{33}=(1/Ne)(\mu_1\mu_4^2)(\mu_3+c\nu_3)^{-2},\quad A_{14}=-(1/Ne)\mu_4[\mu_1(\mu_1-\mu_2)](\mu_1+\mu_2+2c\nu_1)^{-2},\\
&A_{41}=-(1/2Ne)\mu_4[\mu_3(\mu_1-\mu_2)+\mu_4^2](\mu_1+\mu_2+2c\nu_1)^{-1}(\mu_3+c\nu_3)^{-1},\\
&A_{44}=-(1/Ne)\{\mu_1\mu_2[\mu_4^2+2c\nu_1(\mu_3+\nu_3)]+c\nu_1^2[(\mu_1+\mu_2)(\mu_3+\nu_3)-\mu_4^2]\}(\mu_1+\mu_2+2c\nu_1)^{-2}(\mu_3+c\nu_3)^{-1}.
\end{aligned} \tag{B2}$$

APPENDIX C: RELATIONS BETWEEN σ COMPONENTS AND ρ

The following relations between the σ components and the ρ are obtained by solving $\sigma_{ij}\rho_{jk}=\delta_{ik}$ up to terms in B^2. The relations are given here for completeness; aside from notational changes, they are the same as those given by Juretschke.

$$\sigma_{11}{}^0=(\rho_{11}{}^0)^{-1},\quad \sigma_{33}{}^0=(\rho_{33}{}^0)^{-1},\quad \sigma_{23,1}=\rho_{23,1}(\rho_{11}{}^0\rho_{33}{}^0)^{-1},\quad \sigma_{12,3}=\rho_{12,3}(\rho_{11}{}^0)^{-2},\quad S_{11}=A_{11}(\rho_{11}{}^0)^{-2},$$
$$S_{12}=(\rho_{11}{}^0)^{-2}[A_{12}+(\rho_{23,1}{}^2/\rho_{33}{}^0)],\quad S_{13}=(\rho_{11}{}^0)^{-2}[A_{13}+(\rho_{12,3}{}^2/\rho_{11}{}^0)],\quad S_{31}=(\rho_{33}{}^0)^{-2}[A_{31}+(\rho_{23,1}{}^2/\rho_{11}{}^0)],$$
$$S_{33}=A_{33}(\rho_{33}{}^0)^{-2},\quad S_{14}=A_{14}(\rho_{11}{}^0)^{-2},\quad S_{41}=A_{41}(\rho_{11}{}^0\rho_{33}{}^0)^{-1},\quad S_{44}=(\rho_{11}{}^0\rho_{33}{}^0)^{-1}[A_{44}-(\rho_{12,3}\rho_{23,1}/2\rho_{11}{}^0)].$$

APPENDIX D: APPROXIMATE RELATIONS

$$\rho_{11}{}^0\simeq 2/Ne\mu_1(1+2c\nu_1/\mu_1),\quad \rho_{33}{}^0\simeq 1/Ne\mu_3,\quad \rho_{23,1}\simeq 1/Ne(1+2c\nu_1/\mu_1),\quad \rho_{12,3}\simeq 4[\mu_2/\mu_1-c(\nu_1/\mu_1)^2]/Ne(1+2c\nu_1/\mu_1)^2,$$
$$A_{11}\simeq\mu_3/2Ne(1+2c\nu_1/\mu_1),\quad A_{12}\simeq A_{11}+\text{small terms}\simeq(\mu_3+2\mu_2\mu_3/\mu_1+8c\nu_1{}^2\nu_3/\mu_1{}^2)/2Ne(1+2c\nu_1/\mu_1),$$
$$A_{13}\simeq 2\mu_2[(1+2c\nu_1/\mu_1)+2c(4+\nu_1/\mu_2)(\nu_1/\mu_1)^2]/Ne(1+2c\nu_1/\mu_1)^3,\quad A_{31}\simeq c\nu_1/Ne(1+2c\nu_1/\mu_1),\quad A_{33}\simeq(\mu_1/Ne)(\mu_4/\mu_3)^2,$$
$$A_{14}\simeq-\mu_4/Ne(1+2c\nu_1/\mu_1),\quad A_{41}\simeq-\mu_4/2Ne(1+2c\nu_1/\mu_1),\quad A_{44}\simeq-(2c\nu_1/\mu_1)(1+\nu_3/\mu_3)(\mu_2+\nu_1/2)/Ne(1+2c\nu_1/\mu_1)^2.$$

PHYSICAL REVIEW VOLUME 181, NUMBER 3 15 MAY 1969

Pressure and Vacancy-Flow Effects on the Kirkendall Shift in Silver-Gold Alloys*

R. O. MEYER†
University of Arizona, Tucson, Arizona 85721
(Received 23 January 1969)

A series of eight Kirkendall runs plus several supporting measurements were made in silver-gold alloys over the hydrostatic pressure range of 0–8 kbar. Reduction in the size of the Kirkendall shift was found to be due mostly to the effect of pressure on self-diffusion rates, with only about 8% of the reduction being due to changes in the activity-coefficient gradient. Agreement between the magnitude of the measured shift and the predicted value was better than 2%, providing substantial evidence for the validity of the vacancy-flow term in Manning's equation, which constitutes 28% of the total shift. Diffusion porosity was eliminated by the application of pressure for all pressures 10 bar and greater. Evidence was found which indicates that the activation volumes for silver and gold self-diffusion are equal within experimental error.

I. INTRODUCTION

EXPERIMENTS on the effect of pressure on diffusion in solids usually measure a change in the diffusion rate as pressure is increased. From such a change in the self-diffusion coefficient, an activation volume is calculated which is interpreted in terms of relaxation of the crystal lattice under applied pressure.

For an alloy with a concentration gradient, the situation is more complicated than in a homogeneous material. The activation volume alone is not adequate to describe the effect of pressure because diffusion in the presence of a concentration gradient depends on more parameters than those of self-diffusion. In particular, diffusion depends on the chemical activity of the solid solution. Therefore, if the activation volume for self-diffusion is known, a pressure experiment in a concentration gradient will yield information regarding the effect of pressure on the chemical activity of the alloy.

An experiment was designed to measure the Kirkendall shift as a function of pressure at some convenient fixed temperature. Such an experiment would allow us to test Manning's vacancy-flow effect[1] and also measure the effect of porosity on diffusion rates.

Manning considers the effects of various diffusion-driving forces, and for diffusion in a chemical concentration gradient he gets equations similar to Darken's analysis.[2] The differences between Manning's equations and Darken's equations are primarily due to so-called vacancy-flow effects. Several attempts[3–7] have been made to verify Manning's equations, and these attempts have had limited success.

* Supported in part by the U. S. Atomic Energy Commission, Report No. COO-1041-012, through Contract AT(11-1)-1041.
† Present Address: Argonne National Laboratory, Argonne, Ill. 60439.

[1] John R. Manning, *Diffusion Kinetics for Atoms in Crystals* (D. Van Nostrand Co., Inc., Princeton, N. J., 1968), p. 191.
[2] L. S. Darken, Trans. AIME **175**, 184 (1948).
[3] J. R. Manning, Phys. Rev. **116**, 69 (1959).
[4] R. O. Meyer and L. M. Slifkin, Phys. Rev. **149**, 556 (1966).
[5] R. O. Meyer, Phys. Rev. **163**, 641 (1967).
[6] D. J. Schmatz, H. A. Domian, and H. I. Aaronson, J. Appl. Phys. **37**, 1741 (1966).
[7] D. B. Butrymowicz and J. R. Manning, Am. Inst. Mining, Met. Petrol. Engrs., Inst. Metals Div., Spec. Rep. Ser. **2**, 9 (1967).